SAE International®

Numerical and Experimental Investigation of Fuel Effects on Knock Occurrence and Combustion Noise in a 2-Stroke Engine

Fabio Bozza
Universita' di Napoli

Stefano Fontanesi
Universita' di Modena e Reggio Emilia

Alfredo Gimelli
Universita' di Napoli

Elena Severi
Universita degli Studi di Modena

Daniela Siano
Isitituto Motori CNR, Italy

ABSTRACT

Knock occurrence is a widely recognized phenomenon to be controlled during the development and optimization of S.I. engines, since it bounds both compression ratio and spark advance, hence reducing the potential in gaining a lower fuel consumption. As a consequence, a clear understanding of the engine parameters affecting the onset of auto-ignition is mandatory for the engine setup. In view of the complexity of the phenomena, the use of combined experimental and numerical investigations is very promising. The paper reports such a combined activity, targeted at characterizing the combustion behavior of a small unit displacement two-stroke SI engine operated with either Gasoline or Natural Gas (CNG).

In the paper, detailed multi-cycle 3D-CFD analyses, starting for preliminary 1D computed boundary conditions, are performed to accurately characterize the engine behavior in terms of scavenging efficiency and combustion. In order to assess the accuracy of the adopted numerical approach, comparisons between numerical forecasts and experimental measurements of instantaneous in-cylinder pressure histories are carried out for both gasoline- and CNG-fueled engine operations. 3D analyses are also used to investigate the knock sensitivity of the engine to variations of spark timings in a limited set of operating conditions.

The activity is simultaneously developed within a 1D modeling framework, where a detailed quasi-dimensional combustion and knock model is applied to perform a wider investigation of engine performance and knock occurrence for both Gasoline and Natural Gas fuelling. Results from 3D simulations are here used to improve the 1D simulations through a better description of scavenging and combustion processes.

Once validated, 1D analyses are in particular finalized to find the knock-limited spark advance by changing both compression ratio and spark timing in order to reduce the fuel consumption. In this phase, a dedicated routine is also developed to have information on combustion related noise, which may limit fuel consumption improvements. Further confirmations on the validity of the 1D approach to the modeling of the knock onset are derived from full-3D knocking analyses over a limited set of engine operating conditions.

Advantages and limitations of CNG operations of the engine are briefly pointed out at the end of the paper.

INTRODUCTION

Alternative-fueled engines are undergoing a constant growth of interest in the global transportation market as a feasible response to the increase of both pollutant emission limitations and conventional fuel price. In fact, most governments are adopting increasingly limiting regulations on ICE pollutants and fuel consumption as a response to the global warming concern and the connection between hydrocarbon consumption and greenhouse gas emissions. Different "alternative-fuels", ranging from bio-fuels to low-carbon fuels up to hydrogen, are extensively investigated in order to find possible solutions to the above mentioned problems. Among the available options, Compressed Natural Gas (CNG) is one of the most promising possibilities, since it combines low emission levels (mainly CO, CO_2 and highly reactive hydrocarbons) to reduced running costs.

The growing interest towards CNG fueled engines is particularly evident in recently exploded mass transportation markets such as India and south-east Asia, where the environmental issue and the need for low-cost mobility is of crucial importance. In such countries, two-wheel and three-wheel vehicle production has been expanding rapidly over the past several years especially in the urbanized areas. In fact, motorcycles can play an important role in fulfilling both personal and commercial transportation needs in view of the smaller physical size of vehicles, allowing for easier navigation in heavily congested areas. Furthermore, purchase and maintenance are substantially lower than the corresponding costs for even small automobiles, making the types of low-cost motorcycles the most economically efficient transportation option [1].

A major drawback of low-cost motorcycles is that they emit substantial quantities of hydrocarbons (HCs), carbon monoxide (CO), and particulate matter (PM). These pollutants are widely recognized to have significant adverse health effects and deteriorate environmental quality. To address the serious pollution problems posed by two-wheel vehicles, a growing number of countries worldwide have implemented, or are in the process of implementing, motor vehicle pollution control programs aimed at substantially reducing harmful emissions from spark-ignited two-wheel vehicles, as demonstrated by the research efforts paid in this field by important manufacturers [2,3,4].

While waiting for mid-to-long-term fashionable solutions such as electric or hybrid electric motorcycles, CNG appears today to be one of the most promising short-term / low-cost technologies to reduce emission levels while limiting production and running costs.

This is confirmed by the high population of three-wheeled, CNG powered motorcycles in certain Indian cities and some south-east Asia countries as a response to air quality-driven clean-fuel requirements; further diffusion of CNG fueled vehicles on the market is primarily limited by the presence of a capillary network of fueling stations.

Many outstanding contributions dealing either with the development of specifically CNG-fuelled engines or with the conversion to CNG of existing units for automotive applications can be found in literature, while only a few of them deal with two-stroke engines for motorcycles or mopeds [5, 6]. The utilization of the NG within such engines can lead to relevant improvements in NMHC, NOx and CO emissions, despite some challenges can be found in evaporated fuel and unburned HCs. Nevertheless, properly optimized CNG vehicles show potential benefits in both emissions and fuel consumption with reduced cost increase and design modification with respect to, for example, the adoption of more expensive technologies such as direct-injection and/or supercharging.

The development of strategies and technologies for the specific engine application without increasing the R&D costs can profit from robust and accurate computational simulations allowing the researchers to understand and optimize the fundamental processes governing the engine operation. A wide set of both 1D and 3D numerical procedures can be found in literature aiming at carefully modeling the scavenging and combustion processes, as reported for example in [7, 8].

On one hand, 1D tools can be extensively used to assess the influence of both operating and design parameters on engine performance from a global perspective. 1D simulation reduced computational costs allow the researchers to quickly address the global effects of a wide range of solutions and strategies on the overall engine performance; furthermore, 1D tools can provide time-history of pressure and temperature to be used as boundary conditions by the more complex 3D analyses.

On the other hand, full-3D analyses are mandatory whenever point wise flow patterns and geometrical details are needed to accurately understand and optimize the engine behavior. 3D simulation proves to be useful also both in providing 1D simulations input parameters which are difficult to measure at the engine bench and in exploring engine optimization paths which could lead to engine damage at the engine testbed.

Despite coupled 1D-3D simulations are nowadays growing in popularity in the research community, the high computational costs typical of the 3D simulations and the numerical issues arising at the 1D/3D interfaces limit their extensive application to the late development stage.

The paper reports results from a combined experimental and numerical investigation of a two-stroke engine for motorcycle applications. Measurements are used to tune and validate an in-house developed combustion model included in a commercial 1D code, and a commercial CFD tool for the full-3D multicycle analysis of scavenging and combustion.

A preliminary investigation of some engine operations for the CNG-fueled engine are reported in [9], where the advantages in terms of knock resistance of the CNG vs. gasoline were highlighted. The analysis is now extended and improved:

• 1D and 3D data are better integrated and iteratively exchanged in order to improve both the simulation realms;

• a wider set of engine operations, now including gasoline-fueled ones at different engine speeds, is modeled in order to better investigate the effects of the fuel on both combustion evolution and engine performance;

• knock-limit of the engine is further addressed for gasoline fuel; a knock-free operation of the tested engine is confirmed for CNG fuelling;

• a procedure to characterize the combustion related noise of the engine is developed in order to better address the operative limits of the engine.

The numerical models (1D, 3D and combustion noise) are finally used to investigate the engine operative limits under both gasoline and CNG operations. In particular, in order to improve CNG fuelled engine performance, the higher knock-resistance of CNG fuel is exploited through spark advance variations and compression ratio increase. Potential benefits of the adoption of CNG are also verified in terms of combustion related noise.

EXPERIMENTAL ANALYSES

The Engine

As reported in [9], experimental investigations are carried out on a crankcase-scavenged, carbureted, spark-ignited two stroke single-cylinder engine. The engine displacement is 50 cm^3. The engine is shown in Figure 1 below, while Table 1 reports some technical specifications.
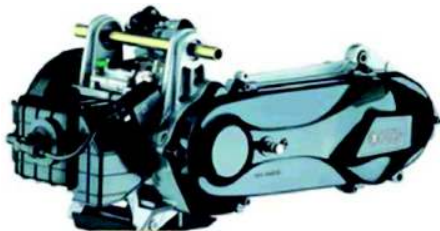

Figure 1. The Morini Engine

Table 1. Engine Specifications

Engine model	Ported Two-Stroke SI
Scavenging type	Schnurle
Displacement	50 cm^3
Compression ratio	11.7:1
Bore, Stroke	41, 37.4 mm
Maximum Power	4.1 kW @8000 rpm
Maximum Torque	4.7 Nm @7500 rpm
Intake Port Open/Number/Width	56° BBDC / 5 / 11 mm
Exhaust Port Open/Number/Width	81° BBDC / 1 / 26 mm

Experimental apparatus

The engine is installed on a DC test bench; both instantaneous and overall sensors are used. Location of the

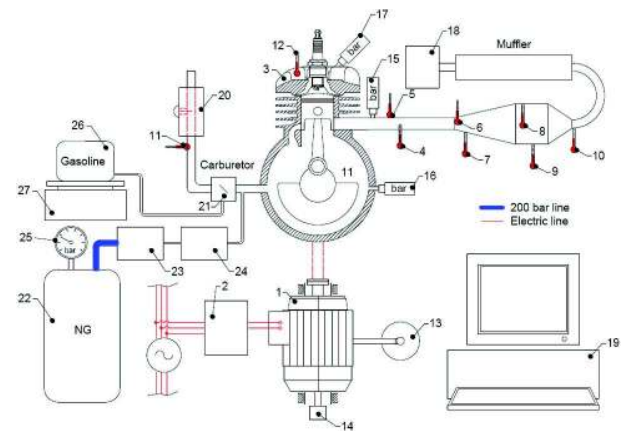sensors and the relative legend are shown in Figure 2 and Table 2 respectively.

Figure 2. Experimental testbed scheme.

Instantaneous pressures inside the crankcase, the cylinder and the exhaust pipe are measured with piezoquartz-transducers at engine speeds ranging from 4000 to 7000 rpm at WOT conditions. To ensure the right functioning of the exhaust piezo-transducer, it is also cooled through a custom-made water circuit. Additional experimental data are collected like: air mass flow rate, torque, speed, fuel flow rate, gas and wall temperatures in a number of sections along the exhaust system. All temperatures are acquired by K type thermocouples.

Table 2. Sensors Legend.

1	DC Electric motor
2	Central Command electric motor
3	Engine
4-12	Thermocouples
13	Force transducer
14	Encoder
15-16	Fast piezoresistive pressure transducer
17	Miniature dynamic pressure transducers
18	Exhaust Analyzer
19	PC + DAQ Card
20	Hot wire anemometer
21	Angular position sensor
22	Gas Tank
23	Natural Gas pressure reducer
24	Natural gas mass flow meter
25	Pressure Gauge
26	Petrol tank
27	Balance

The air mass flow rate measurement is carried out by a customized hot film anemometer. The sensor and the electronic circuit of a commercial anemometer are placed into a new suitable custom-made structure in order to ensure accurate measurement despite the low air flow rate. The device is calibrated with stationary tests in comparison with a more accurate mass flow rate measurement.

At each operation point, the engine is fuelled with both gasoline and CNG. The latter is injected in the intake pipe

upstream the crankcase, at a moderate over-pressure above the atmospheric one. NG flow rate is adjusted through an electronic control valve, incorporated in the NG mass flow rate meter (Bronkhorst F202AC).

NG tests are carried out approximately at the same air index ($\lambda = \alpha/\alpha_{st}$) provided by the standard carburetor in the gasoline tests. To reduce variations in operating conditions, the NG fuelling test is performed immediately after the gasoline one. During the test the air index is firstly checked by the hot film anemometer for the air mass flow rate; this value is then adjusted by post-processing data from exhaust gas emissions measurements.

The injection of a gaseous fuel is expected to reduce the air flow rate and power output. The latter is in particular due to the combined effects of the lower fuel flow rate and slower NG laminar flame speed. A partial compensation is due to the slightly higher lower heating vale of the CNG (45471 kJ/kg) with respect to the gasoline fuel (43700 kJ/kg). The slower NG combustion also indicates the need to adapt the spark timing to the CNG fuelling. However, due to limitations of the experimental equipment, CNG tests are carried out at the same spark timing of Gasoline one.

The collected data are used to validate both 1D and 3D models. Then, in order to improve CNG operation, the validated models are employed to analyze variations in the spark timing and compression ratio. In the following, experimental data and numerical results always refer to WOT operation and same air index for gasoline and CNG.

COMPUTATIONAL METHODS

1D model - whole engine analysis

Combustion Model

1D analyses are carried out with GT-Power® commercial product [10]. A in-house developed combustion model is however utilized, exploiting the "user model" features of the GT-Power code. Differently from the standard combustion model, relying on a two-equation entrainment model [11], the developed approach applies to the "wrinkled flamelets" combustion regime. The latter is widely recognized to be the one really occurring inside internal combustion engines [12,13]. In the wrinkled flamelets regime the flame front is corrugated by the convective action of turbulent eddies which determine an increase in the flame front area and burning rate. The model, extensively described in [14,17,18,19,20] is based on a fractal schematization of the flame front surface and covers the different burning phases occurring during the overall reaction process, namely: flame initiation, laminar burning, turbulent burning, and wall combustion.

In the model, mass burning rate, dm_b/dt, is computed as a function of the flame front increase area A_T/A_L:

$$\frac{dm_b}{dt} = \rho_u A_T S_L = \rho_u \left(\frac{A_T}{A_L}\right) A_L S_L$$

(1)

Following the fractal geometry concepts, the above area ratio can be expressed in terms of the ratio of maximum and minimum wrinkling scales, L_{max}-L_{min}, and fractal dimension D_3:

$$\left(\frac{A_T}{A_L}\right)_{fr} = \left(\frac{L_{max}}{L_{min}}\right)^{D_3 - 2}$$

(2)

In eq. (2), the instantaneous flame radius and the Kolmogorov length scales are chosen as the maximum and minimum wrinkling scales, respectively. The D_3 dimension indeed depends on the ratio between the turbulence intensity u' and the laminar flame speed S_L [15]. Proper laminar flame speed correlation, holding for both Gasoline [16] and Methane [21] fuels, are included in the model.

Eq. (2) is the classical formulation of a fractal combustion model [12,13,16], while in the present paper, two main modification are introduced, both important in two-stroke engine operation. In a small-size two-stroke engine, in fact, the rotational speed may be as high as 10.000 rpm. At high engine speeds, however, the flame wrinkling determined by the turbulent flow field can be so intense to stretch and break the flame, producing a multiple connected flame front, with "islands" of unburned mixture trapped within the burned gas zone. In this case, the combustion regime enters the "distributed reaction zone". This occurs when the "Karlovitz number", Ka, exceeds the unity. On this basis, it is introduced a correction term in the fractal burning rate expression (2). For $Ka>1$, the laminar flame area is slightly enhanced to account for the additional reaction zone due to the presence of the unburned mixture pockets:

$$\frac{A_T}{A_L} = \left(\frac{A_T}{A_L}\right)_{fr} \cdot \Lambda_1 \qquad \Lambda_1 = \left(1 + w_{turb} k_{AL,1} Ka\right)$$

(3)

The following definitions of Karlovitz Number, Ka, Damkholer Number, Da, and flame thickness, δ_f, are utilized in the model:

$$Ka = \frac{(u'/S_L)^{\frac{3}{2}}}{(L_I/\delta_f)^{\frac{1}{2}}} = \frac{(u'/S_L)}{(Da)^{\frac{1}{2}}} \qquad Da = \frac{L_I/\delta_f}{(u'/S_L)} \qquad \delta_f = \frac{v_u}{S_L}$$

(4)

L_i being the integral length scale, δ_f the flame thickness and v_u the kinematic viscosity of unburned gas zone. The correction coefficient $k_{AL,1}$ is usually in the range (0.0 - 0.1), while the weight w_{turb} in eq.(3) allows to gradually apply the correction during laminar-turbulent flame transition (w_{turb} going from 0 to 1). The above correction is activated only for $Ka>1$, which may occur at high speeds (high u') and/or low loads (low S_L). A high residual gas fraction, typical of two-
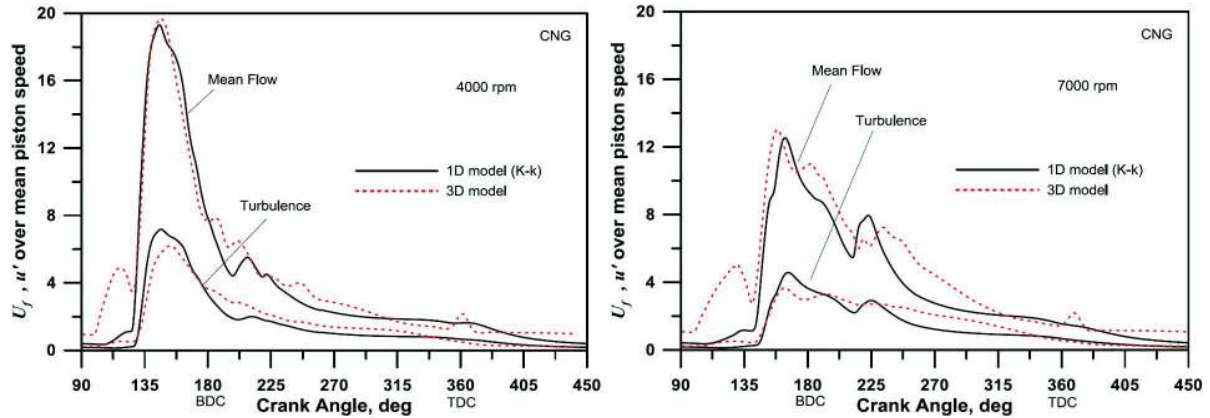
Figure 3. In-cylinder average gas velocity and turbulence intensity - 4000 and 7000 rpm, CNG fuel.

stroke engines, is also responsible for a low S_L and increased Ka.

A further modification is required in engines where a relevant flame distortion is expected. This once again occurs in a ported two-stroke engine, where the very intense mean flow motion produced during scavenging process is conserved in a greater extent at spark time. Flame distortion is expected to be higher for higher mean flow motions (U_f) and lower turbulent flame speeds (S_T). For this reason, a reasonable correction is proposed, as shown:

$$\frac{A_T}{A_L} = \left(\frac{A_T}{A_L}\right)_{fr} \cdot \Lambda_1 \cdot \Lambda_2 \qquad \Lambda_2 = \left(1 + w_{turb} k_{AL,2} \frac{U_f}{S_T}\right)$$

(5)

$$S_T = S_L \left(\frac{A_T}{A_L}\right)_{fr}$$

(6)

Mean flow velocity U_f is derived by the integration of the K equation, presented in next paragraph. The tuning coefficient, $k_{AL,2}$, is of order 0.0 - 0.2.

Turbulence Model

Wrinkling scales in eq. (2) are computed as a function of the characteristics of the turbulent flow field inside the cylinder, utilizing a two-equation K-k approach [22,23].

$$\frac{dK}{dt} = c_{in}\frac{1}{2}\dot{m}_{in}u_{in}^2 + c_{ex}\frac{1}{2}\dot{m}_{ex}u_{ex}^2 - P - K\frac{\dot{m}_{ex}}{m} + c_{tmbl}K\frac{\dot{\rho}_u}{\rho_u}$$

$$\frac{dk}{dt} = P - D - k\frac{\dot{m}_{ex}}{m} + c_{tmbl}k\frac{\dot{\rho}_{cyl}}{\rho_{cyl}}$$

$$P = c_P\frac{K}{t'} \qquad D = c_D\frac{k}{t'}$$

$$\left(K = \frac{1}{2}mU_f^2\right) \quad \left(k = \frac{3}{2}mu'^2\right) \quad \left(t' = \frac{L_I}{u'}\right) \quad \left(L_I = c_i\sqrt[3]{V}\right)$$

(7)

In the above balance equations, K is the kinetic energy of the mean flow field (U_f) - whose production is mainly related to the intake and exhaust flow rates ($\dot{m}_{in}$ and $\dot{m}_{ex}$) - k is the kinetic energy of the turbulent flow field (assumed homogeneous and isotropic), while D is its dissipation rate. P represents a turbulent production term, which characterizes the energy transfer between the mean and the turbulent flow field (*energy-cascade* mechanism). Density variation terms, in the unburned and whole cylinder zones, account for turbulence enhancement/decay due to tumble vortex compression/expansion, weighted by a tuning constant, c_{tmbl}. Turbulence production and dissipation rates are defined through simple expressions, including two additional tuning constants c_P and c_D. The turbulence intensity is derived from the k definition. The integral length scale L_I is evaluated as a characteristic dimension of the instantaneous cylinder volume, and, consequently, the Kolmogorov length scale can be estimated (for isotropic turbulence), as:

$$l_k = \frac{L_I}{\text{Re}_t^{3/4}} \qquad\qquad \text{Re}_t = \frac{u'L_I}{v_u}$$

(8)

To select proper values of tuning constants in eqs. (7), preliminary 3D analyses are carried out - with boundary conditions provided by the 1D code - to characterize in-cylinder mean flow velocity and turbulence levels at different engine speeds. As an example, extracted data for the 4000 and 7000 rpm engine speeds, CNG fuel, are reported in Figure 3. As visible in the plots, in-cylinder average mean gas velocity and turbulent fluctuations - non-dimensionalized respect to the mean piston speed - show a similar trend (dashed profiles), reaching a peak level toward the end of the induction stroke, and rapidly decaying during the compression. Turbulence decay is faster than mean flow energy decay, reaching a very low value a few degrees BTDC.

Figure 3 in particular show that a unique set of tuning constant for eqs. (7) is able to correctly reproduce the 3D turbulence results with a good accuracy at different engine

speeds. Similar results were obtained for different engine speeds and for gasoline fuel, as well.

Scavenging Model

As known, a classical limitation of 0D models is the possibility to correctly describe the scavenging process: the actual mixing between the incoming mixture and burned gases, and the short-circuiting at the exhaust in fact hardly depend on the in-cylinder 3D flow distribution, port geometry and operating conditions [24,25]. To handle these complex phenomena, GT-Power code includes a simplified approach, where a "Scavenging Law" is assigned in input. This profile quantifies the amount of burned products exhausted at the port as a function of the instantaneous in-cylinder residual fraction. Once again, to overcame the 0D limitations, preliminary 3D analyses are utilized and processed to derive a 3D computed scavenging law, as shown in Figure 4. The latter puts into evidence that, initially, the scavenging behaves similarly to a 'perfect-displacement' of burned gases, while later during the process the contemporary presence of mixing and short-circuiting phenomena determine a sudden decrease of the exhaust residual ratio. Even if the shown profile may vary with fuel type and operating conditions, it was verified that differences are negligible and a single scavenging law was actually utilized in 1D analyses at each speed and for both fuels.
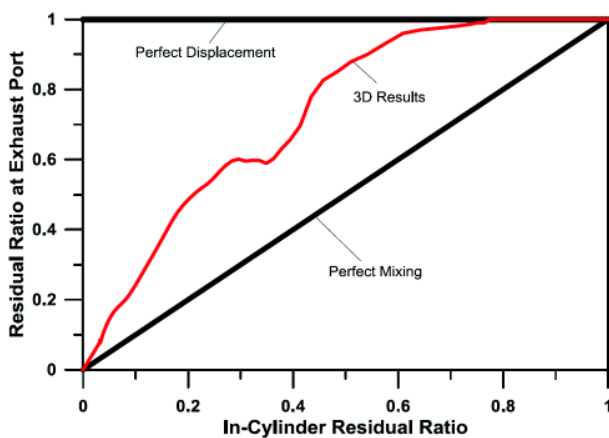

Figure 4. 3D computed scavenging law utilized in 1D analyses

1D-3D interaction

As discussed, 1D model accuracy is greatly enhanced in terms of both turbulence characteristics and scavenging profile, thanks to 3D modeling. This allows to accurately predict overall engine performance and intake and exhaust pressures to be used as boundary conditions for the 3D tool. An iterative exchange of information is hence required between the two modeling approaches. Of course, the loop between 1D and 3D simulation tools is performed until differences in terms of key-parameter predictions are negligible.

1D knock model

A further feature of the 1D model is the presence of a procedure accounting for knocking onset. It is based on the solution of a kinetic scheme in the unburned gas zone, whose thermodynamic conditions are defined by the previously described combustion model. For Gasoline operation, a reduced kinetic mechanism for the oxidation of iso-octane and n-hepthane mixtures is employed. It was developed by Tanaka and Keck [26] and includes 5 elements, 32 species and 55 reactions. The mechanism handles both low and high temperature reactions and is particularly tuned to reproduce the end-gas conditions in a SI engine. For NG fuelling, the GRI-Mech 3.0 mechanism [27] is indeed utilized (5 elements, 53 species and 325 reactions).

The solution of the chemical kinetic scheme allows to compute variations on unburned species concentration (dx_i/dt) and the related heat released, dQ_{chem}/dt [9,23]. Unfortunately, the 0D treatment of the in-cylinder process doesn't allow to reproduce high-frequency knock-induced pressure oscillation. For this reason, to quantify knock occurrence and intensity, it is not possible to resort to classical knock indices (*MAPO, IMPO or DKI* - which will be indeed considered in the 3D section). Nevertheless, it is possible to defined a parameter, x_{Qub}, estimating the percentage of fuel's chemical heat released in the unburned zone during autoignition, as:

$$\frac{dQ_{chem}}{dt} = -m_u \sum_{i=1}^{N_{spec}} e_i \frac{dx_i}{dt} \qquad x_{Qub} = \frac{\int \frac{dQ_{chem}}{dt}dt}{m_f LHV}*100$$

$$(9)$$

Previous investigations [23] showed that a reliable threshold value for knocking onset is about 2%. In the following analyses, the spark timing is advanced until the above value is overcome, so defining the 'knock-limited' spark advance.

Combustion noise model

Besides the knocking onset, another important phenomenon which may limit the maximum spark timing is the combustion radiated noise. Spark advancing in fact determines an increase in pressure rise rate, directly related to the external radiated noise [28]. For this reason a procedure is developed to quantify the effects of the combustion characteristics on overall noise, for the engine under test operated with either Gasoline and Natural Gas (CNG).

Radiated engine noise, as known, is due to engine structural vibration induced by the in-cylinder pressure exciting the engine structure, and directly causing it to vibrate and radiate noise (direct combustion noise) [28,29]. Actually, the overall noise also includes a mechanical contribution (primary and secondary mechanical noise), produced by moving parts and associated with small impacts due to the crankshaft mechanism, including pistons, connecting rods, camshaft, etc. The analysis of the mechanical noise is beyond
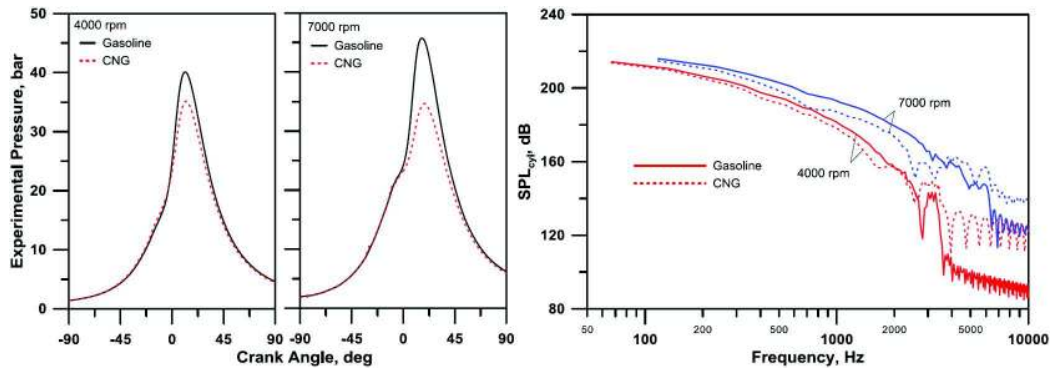
Figure 5. Experimental Pressure and SPL at 4000 to 7000 rpm, WOT operation, for Gasoline and CNG

the scope of the present analysis and it is assumed to be a constant in model.

As said, direct combustion noise is due to the rapidly fluctuating cylinder pressure forces, but it is also depending on the attenuation characteristics of the engine block. The combustion excitation is related to the shape, magnitude and repetition of the cylinder pressure rise and, consequently, any change to the combustion process, due as an example to a different injected fuel, affects the combustion noise, too. The proposed approach is based on the 'attenuation curve', in which a relationship between the in-cylinder Sound Pressure Level (*SPL*) and radiated noise level is established.

The first step of the analysis is the computation of the frequency contents of the experimentally measured pressures, through the employment of a Fast Fourier Transform (FFT). The SPL is then defined as:

$$SPL_{cyl} = 20\log_{10}\left(\frac{\tilde{p}}{p_0}\right)$$

(10)

where p_0 is the standard reference level of $2\ 10^{-5}$ Pa, and $\tilde{p}$ denotes the effective value of the pressure signal:

$$\tilde{p} = \sqrt{\frac{1}{T}\int_0^T p(t)^2\,dt}$$

(11)

As an example, Figure 5 shows the experimental pressure traces at 4000 and 7000 rpm, at WOT condition, for gasoline and CNG, and the related *SPL* up to 10000 Hz.

As expected, at each engine speed, the CNG fuel exhibits a slower burning rate and a lower pressure peak than Gasoline. Consequently, the in-cylinder *SPL* at both speed is reduced. The slightly higher high frequency content (above 4000 Hz) does not contribute too much at the overall radiated noise.

The latter, as already said, depends on structural attenuation of the engine block, assumed to behave as a linear system. Under the additional hypothesis of free field conditions, the external sound pressure level (*SPL$_{ext}$*), at 1m from the engine, can be written as:

$$SPL_{ext}(dBA) = SPL_{cyl}(dB) + SA(dB) + AW(dB)$$

(12)

In the above equation, *SA* term represents the engine Structure Attenuation, shown in Figure 6. Although, not exactly referring to the tested powertrain, the considered profile accounts for strong attenuation at low and high frequency range, as verified in most of the actual internal combustion engines [28]. In addition, since the same profile is utilized for both gasoline and CNG, the relative difference of radiated noise between the two fuels is expected to be well captured.

In order to obtain an output in dBA, an additional filtering is applied using the A-Weighting (*AW*) filter reported in the same Figure 6, which takes into account the human ear perception.

Repeating the above described procedure for each experimental pressure cycle, the external radiated noise resulting from eq. (12) can be easily predicted, as shown in Figure 7a. Due to uncertainties in the specification of the *SA* profile in Figure 6, the maximum in-cylinder pressure rise rate ($dp/d\theta_{max}$, bar/deg) is also reported as a function of engine speed and injected fuel (Figure 7b). Both Figures clearly confirm that CNG operation is quieter at each operating condition. In particular, the effects of slower CNG combustion increase with the engine speed (see Figure 5) determining a reduced noise emission at high speeds.

Figure 7a also shows that maximum radiated noise, for gasoline combustion, approaches 103 dBA. In further analyses related to engine optimization in CNG operation, the latter value will be hence considered as the maximum admissible noise level.

3D model - Detailed in-cylinder analysis

Computational Grid

3D-CFD in-cylinder simulations are carried out using Star-CD licensed by CD-Adapco; the mesh is generated through the es-ice tool and is made up of mainly hexahedral cells which are progressively distorted, activated and deactivated to account for the piston motion. The
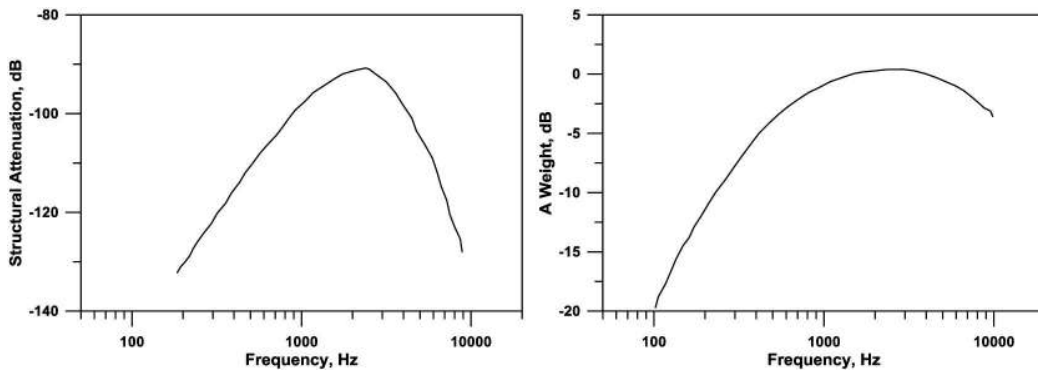
Figure 6. Typical engine structure attenuation (a) and A-Weighting for human perception (b)
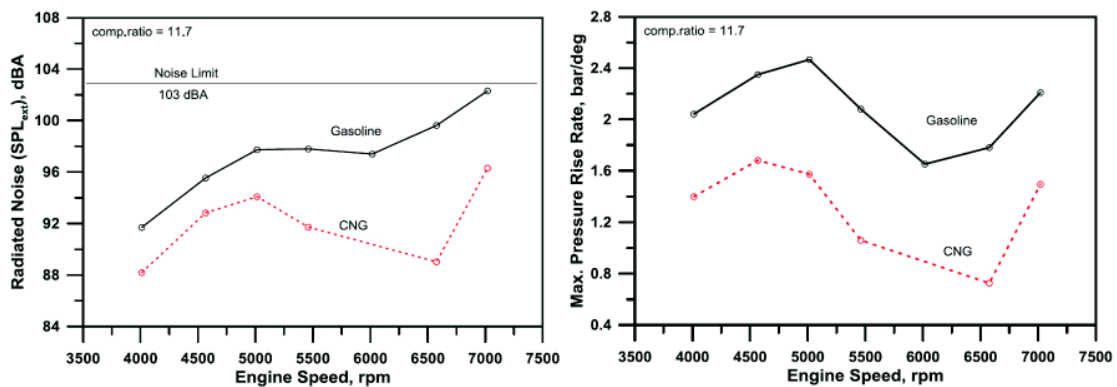

Figure 7. Predicted Combustion Noise (a) and maximum pressure rise rate (b): Gasoline vs CNG at WOT

computational domain covers the combustion chamber and in-head pipe portions. Thanks to the full symmetry of the domain, only half of the engine is modeled in order to reduce the computational cost of the simulations.

Particular attention is paid to the grid morphology, in order to minimize cell distortion and limit numerical instabilities arising from the presence of poor quality cells. The port portion of the grid is generated though a mapping process leading to a mesh of regularly-shaped and flow-oriented hexahedra, while the combustion chamber grid is the results of a trade-off between grid size and ability to capture even the smallest relevant geometrical features. As a result, 550000 cells are used to model the engine at BDC and nearly 325000 are used at TDC. Some key features of the grid are reported in Figures 8 below.

Gas exchange between the cylinder and the ports is performed through activation/deactivation of the communication of arbitrarily adherent cells, where a closed port tolerance equal to 0.05 mm is introduced to limit numerical instabilities at closures and openings.
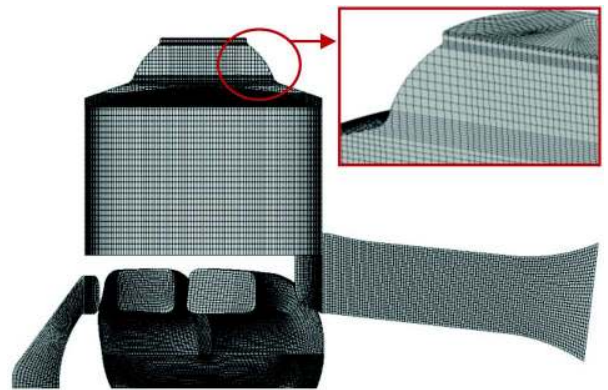

Figure 8. Details of the cylinder mesh

CFD Setup

As reported in [9], each engine cycle starts at 90°CA after Firing Top Dead Center (hereafter AFTDC), i.e. a few crank angle degrees before the exhaust port opening, and covers the full 360°CA.

Boundary conditions are derived from the 1D model of the engine, as well as the spatially uniform initial conditions for the very first engine cycle. Particularly, time history of both pressure and temperature are imposed at both the intake and exhaust pipes in order to adequately take into account the ramming effects, which strongly influence the scavenging performance of the engine.

As for the gas composition, experimental measurements at the engine tailpipe are used to impose the mass fractions at the beginning of the first engine cycle. Among the exhaust gases, only those relevant for the adopted combustion model, which is briefly described in the subsequent section, are used, while the remaining of the species is re-assigned to N_2. Since all the simulations are carried out through several subsequent engine cycles, such initial gas composition is expected to play a negligible influence on the obtained results. Cell-to-cell gas composition at the end of each cycle is then mapped onto the subsequent cycle by means of a user-defined Fortran routine. As far as the fluid properties are concerned, ideal gases with temperature dependent properties are chosen; concerning turbulence modeling, the realizable k-ε model in its high-Reynolds formulation is chosen as a closure model. Heat transfer through the cylinder walls is accounted for by setting fixed temperatures on the different wall regions and using the heat transfer model by Angelberger et al. [30].

Variable time steps according to the cycle events are set, ranging from 0.1°CA during intake and compression down to 0.02°CA during the early openings / late closures of the ports and during the main combustion events. Finally, 2nd order accurate MARS scheme is used for the momentum and turbulence equations, while Central differencing is used for the energy equation. Algebraic Multi Grid solver (AMG) is adopted to speed up the calculations.

Combustion model - ECFM-3Z

The main advantage of the adopted combustion model is the ability to combine combustion sub models for each of auto-ignition, premixed propagating flame and diffusion flame regimes which may simultaneously occur inside modern IC engines.

The model takes into account the local sub-grid state of the gases, i.e. their composition and temperature, by applying a simple form of double conditioning (for each of mixing and reaction states) to the cell mean values solved by the transport equations in CFD simulations [31,32,33]. For the specific aim of the present paper, ECFM-3Z is adopted for its ability in simultaneously modeling both premixed combustion and auto-ignition due to knocking.

ECFM-3Z knock model

Among the many scalars used by the ECFM-3Z model, one, named *YIG* within the Star-CD implementation, is devoted to the analysis of auto-ignition. This passive scalar, which is transported by the local flow, does not take part into the combustion reactions, and is used to trace the occurrence of pointwise thermodynamic and mixture conditions favorable to knock. *YIG* concentration in each computational cell is dependent on the anti-knock fuel characteristics through the equation below.

$$\frac{dYIG}{dt} = YTF * f(\tau_d)$$

(13)

$$\tau_d = a*(RON/100)^b * \left(\frac{P}{1+Yegr}\right)^e e^{\frac{g}{T_u}}$$

(14)

where *a, b, c, g* are model constants *YTF*, *Yegr* and *P* are the local cell fuel fraction, residual gas fraction and pressure respectively and T_u is the temperature of the unburned gases. Knock occurs whenever *YIG* concentration is greater than the fuel tracer concentration, giving rise to the rapid development of a new local flame kernel.

Knock tendency evaluation

From an experimental point of view, the determination of knock onset is usually entrusted to the analysis of data by accelerometers or cylinder pressure sensors. However, most knock indices are extracted from the in-cylinder pressure signal because of its direct connection with knock phenomena.

The two most established indices used to define the knock intensity/tendency are [34]:

• *MAPO*: Maximum Amplitude of Pressure Oscillations, which is related to the pressure oscillation peak due to knock;

• *IMPO*: Integral of Modulus of Pressure Oscillations, which is a way to represent the energy contained in the high frequency pressure oscillations due to knock.

Both this parameters are based on the pressure trace as an input, so that they represent suitable indices for the analysis of the data extracted from the 3D simulations. They can be expressed as:

$$IMPO = \frac{1}{N}\sum_1^N \int_{ST}^{ST+W} |\tilde{p}| d\theta$$

(15)

$$MAPO = \frac{1}{N}\sum_1^N \max_{ST,ST+W} |\tilde{p}|$$

(16)

where *N* is the number of computed cycles, *ST* is the spark timing in crank angle degrees, *p* is the filtered pressure and *W* is the width of the reference computational window.

The onset of knock is determined whenever one of the two above indices exceed a user-defined threshold value: previous works in literature [34, 35], show that either *MAPO* or *IMPO* can be alternatively used as knock indices.
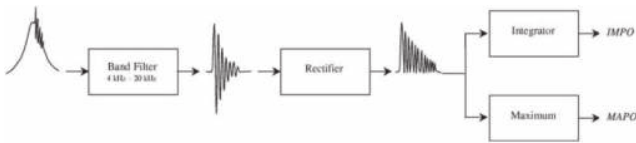
Figure 9. Sketch of MAPO/IMPO evaluation [34]

Using either *MAPO* or *IMPO* the threshold level beyond which we can assume that knock occurs depends on both the engine operative conditions and the frequency of the adopted band-pass filter. From a combination of the two indices, a Dimensionless Knock Indicator can be defined:

$$DKI = \frac{IMPO}{MAPO * W}$$

(17)

DKI is then seen as ratio between two surfaces: the former (*IMPO*) is the surface under the pressure signal while the latter (*MAPO*W*) is the overall surface of the computational window. As a consequence, the *DKI* represents the "weight" of *IMPO* within the computational window.

A *DKI* lower limit of 0.2 was identified in [34], and this value is employed in the present paper to evaluate the knock tendency of the investigated engine.

Scavenging coefficients

Preliminary analyses of the scavenging performance of the engine are used to validate the accuracy of the 3D simulations, in view of the importance of an accurate representation of the gas exchange process to correctly model the combustion evolution. The characterization of the scavenging process over a wide range of engine speeds and for both gasoline-and CNG-fueled operations is therefore performed using well-established coefficients found in literature [24, 25]: Delivery ratio (*DR*), Charging efficiency (*CE*), Retaining (or Trapping) efficiency (*RE*) and Scavenging efficiency (*SE*). The definition of the above parameters is reported in the Appendix A section at the end of the paper.
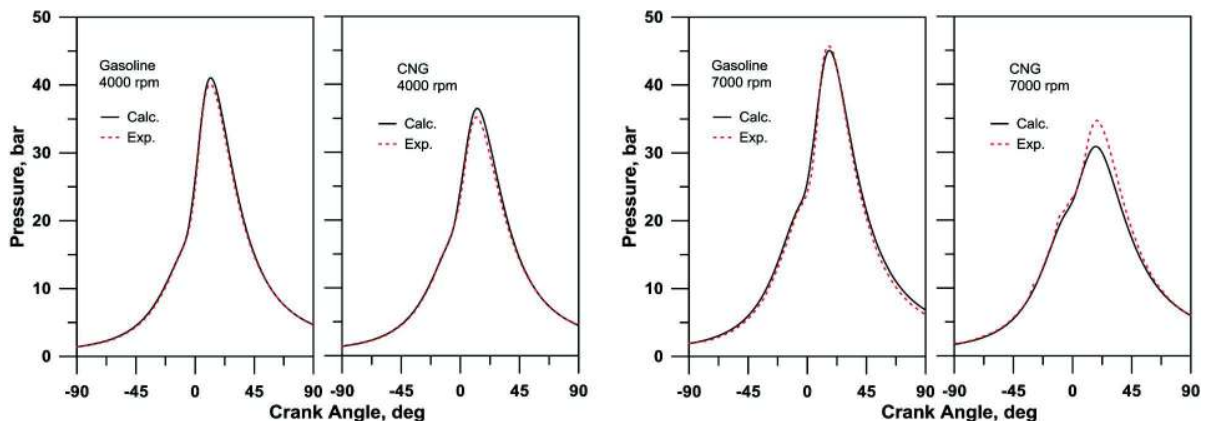
RESULTS

1D results: whole engine performance

The 1D model of the whole engine is preliminarily validated against experiments in terms of overall performance. Figure 10 highlights the expected decrease on mechanical power output due to CNG fuelling. Computed results are in very close agreement with experimental data, especially at low and medium engine speeds.
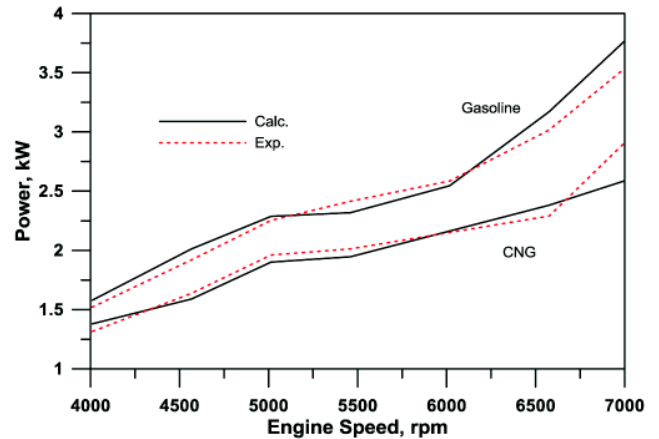

Figure 10. Computed and Measured Power Output

The described exchange of information between 1D and 3D models allows to improve 1D model accuracy during both scavenging and combustion phases, as demonstrated in Figures 11 and 12. In particular, the developed combustion model is able to correctly reproduce the closed port period of the thermal cycle by changing injected fuel and engine speed, thanks to an accurate prediction on in-cylinder turbulence field (Figure 3). A slightly worst agreement is only found at 7000 rpm for CNG operation, mainly due to the presence in the experimental data of a very large cycle-by-cycle variation, induced by the slower CNG burning speed.

In addition, the availability of the 3D computed scavenging law guarantees a precise forecast of in-cylinder
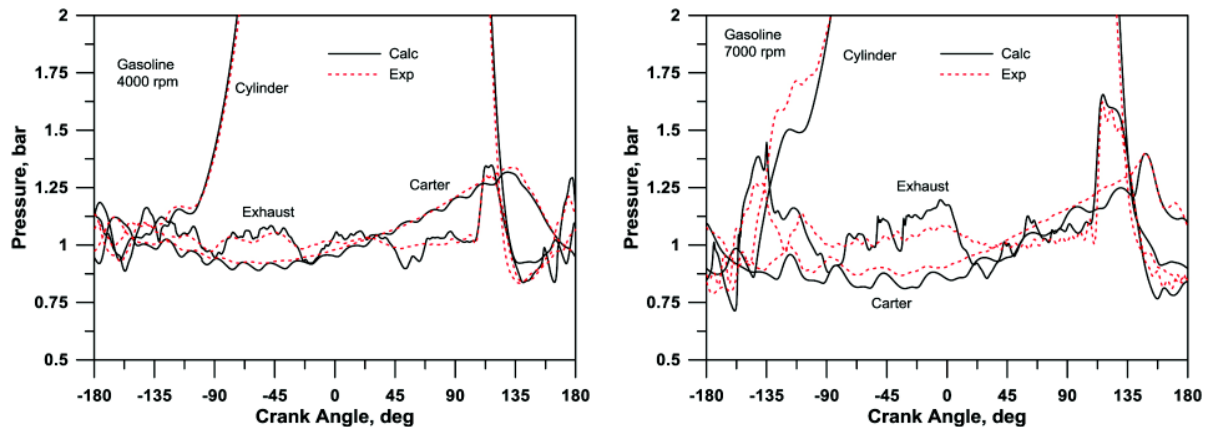

Figure 11. In-Cylinder Pressure @ 4000 and 7000 rpm, WOT operation, for Gasoline and CNG.

Figure 12. Carter, Cylinder and Exhaust Pressure @ 4000 and 7000 rpm, WOT operation, Gasoline.
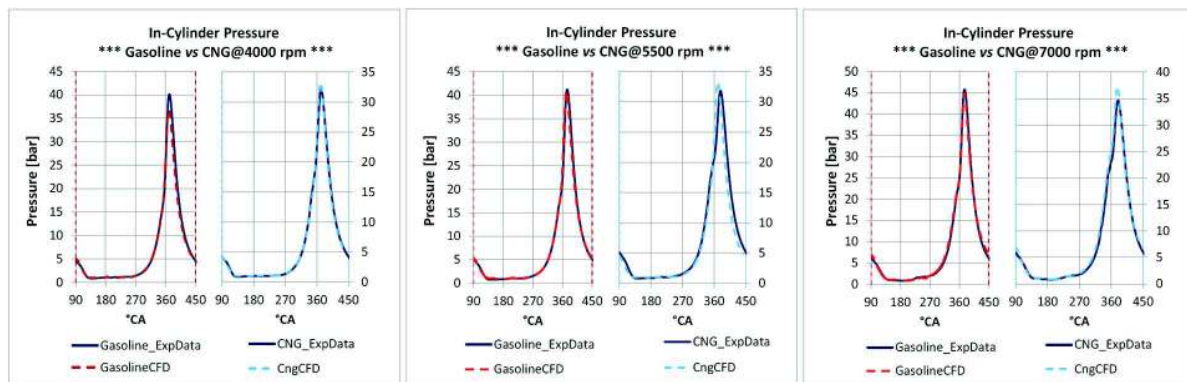

Figure 13a. CFD Pressure vs. experiments for both fuels at different engine speeds

composition, affecting the laminar flame speed and combustion rate. Cylinder filling conditions are very well captured thanks to an accurate description of pressure pulses and ramming phenomena in the intake and exhaust ducts, as shown in Figure 12. Similar results were obtained at each analyzed engine speed, finally determining the correct trends in terms of overall performance in Figure 10.

3D results - scavenging and combustion

As reported in [9], the 3D CFD combustion analyses are preceded by a wide set of investigations to determine the minimum number of subsequent engine cycles to reach both a periodic engine condition and a stable scavenging behavior, i.e. the onset of constant scavenging coefficients. In order for the calculations to reach a satisfactory periodic convergence, a minimum of seven subsequent engine cycles are simulated for each operation.

Information from both the CFD tools are iteratively exchanged until differences in terms of key-parameter predictions are negligible, in order to improve the accuracy of the numerical forecasts:

• the 1D model is at first used to provide time-varying boundary conditions in order to correctly capture the gas-dynamic behavior of the engine;

• after the onset of a cyclic repeatability, 3D derived time-dependent in cylinder data are extracted for each tested condition and used as tuning and validation data within the 1D combustion model described above. The data cover average gas velocities, turbulence intensity, integral length scales, turbulent kinetic energy and dissipation rate, cumulative burned fraction in both the cylinder and the exhaust pipe;

• the tuned 1D model is again used to provide more accurate boundary conditions for the 3D simulations.

Both CNG- and gasoline-fuelled conditions are modeled for three revving speeds and under the same air to fuel ratio.

A further confirmation of the validity of the numerical process comes from the observation of Figures 13a, 13b and 14 below, where in-cylinder pressure, IMEP and scavenging coefficients are respectively reported for all the investigated conditions. The following issues can be highlighted:

• from a general perspective, the use of the iterative 1D / 3D numerical procedure allows all the numerical forecasts to

closely match the experimental counterparts. This is particularly evident for the scavenging coefficients, where both the absolute values and the trends are correctly captured;

• the calculated in-cylinder pressure traces are also correctly superimposed to the experiments, where a slight pressure peak overestimation can be detected only for the CNG-fuelled cases;

• as expected, comparing gasoline operations to their CNG counterparts under the same air index, the effect of the reduced CNG mass-specific energy leads to a general downgrade of the in-cylinder pressure trace and, consequently, to a reduction on the Indicated Mean Effective Pressure. This confirms the well-known decrease of engine performance when CNG replaces gasoline without any substantial further modification to the engine operating conditions.
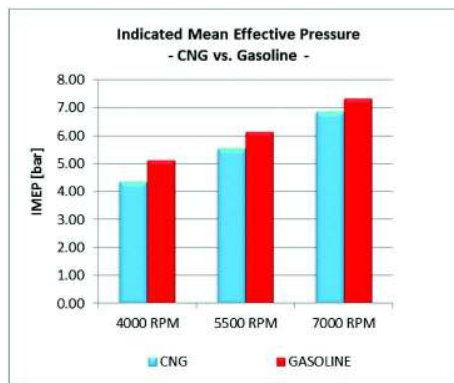

Figure 13b. Calculated Indicated Mean Effective Pressure for both fuels at different engine speeds

The picture sequence reported in Figure 15 below shows a comparison between gasoline and CNG operations of the engine in terms of combustion progress variable for a revving speed of 7000 rpm. From a qualitative perspective, negligible differences can be observed for the two fuels in terms of flame front evolution within the combustion chamber throughout the early stages of the combustion, although higher peak values are visible for the gasoline operation. It is only towards the mid stage of the combustion (i.e. 16°CA ASI) that the gasoline combustion shows an enhanced combustion progress in terms of both flame front spatial extension and reaction progress peak values.

The faster growth of the flame front for the gasoline-fueled case leads to an improved efficiency of the combustion process, and therefore to an increase of engine performance. This observation is further confirmed by the analysis of the pressure rise reported in Figure 16 below, where the steeper increase of the gasoline operation (red curves) clearly emerges.

A comparison between the three engine speeds for the gasoline-fueled operation is reported in Figure 17 below, where turbulence intensity is reported.

A sequence of pictures highlighting the combustion evolution for the gasoline operation and for the three engine speeds is reported Figure 18 below. Fuel consumption is depicted through the evaluation of the ratio of the local fuel fraction over the fuel fraction peak just before the spark ignition, in order to disregard differences in terms of both local and global A/F values among the three engine speeds. It is widely recognized that the initial stages of the combustion process are primarily dominated by a combination of local equivalence ratio values at the spark plug and in-cylinder temperature; it is in fact well established that in-cylinder turbulence and local flow patterns play a negligible role on the early flame development. Comparing the three engine speeds, it is possible to observe that:

• the 4000 rpm case shows the highest in-cylinder temperature levels (872 K) at ignition, together with nearly-stoichiometric / slightly lean mixture composition (λ=1.05),
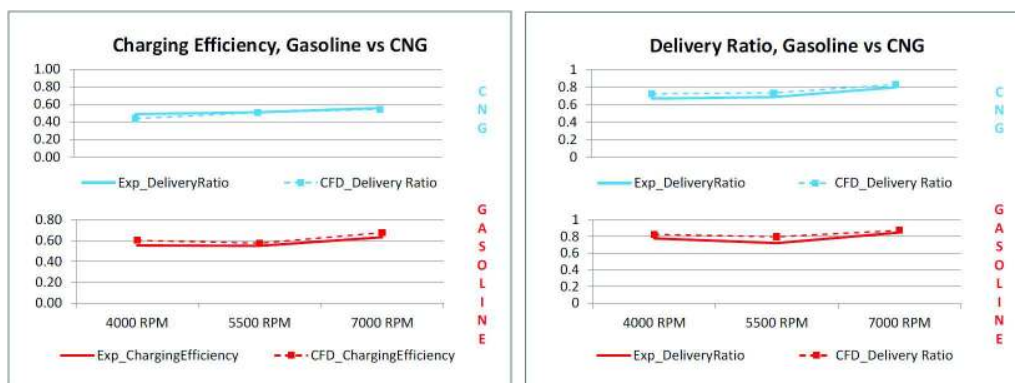

Figure 14. CFD Scavenging Parameters vs. experiments for both fuels and different engine speeds
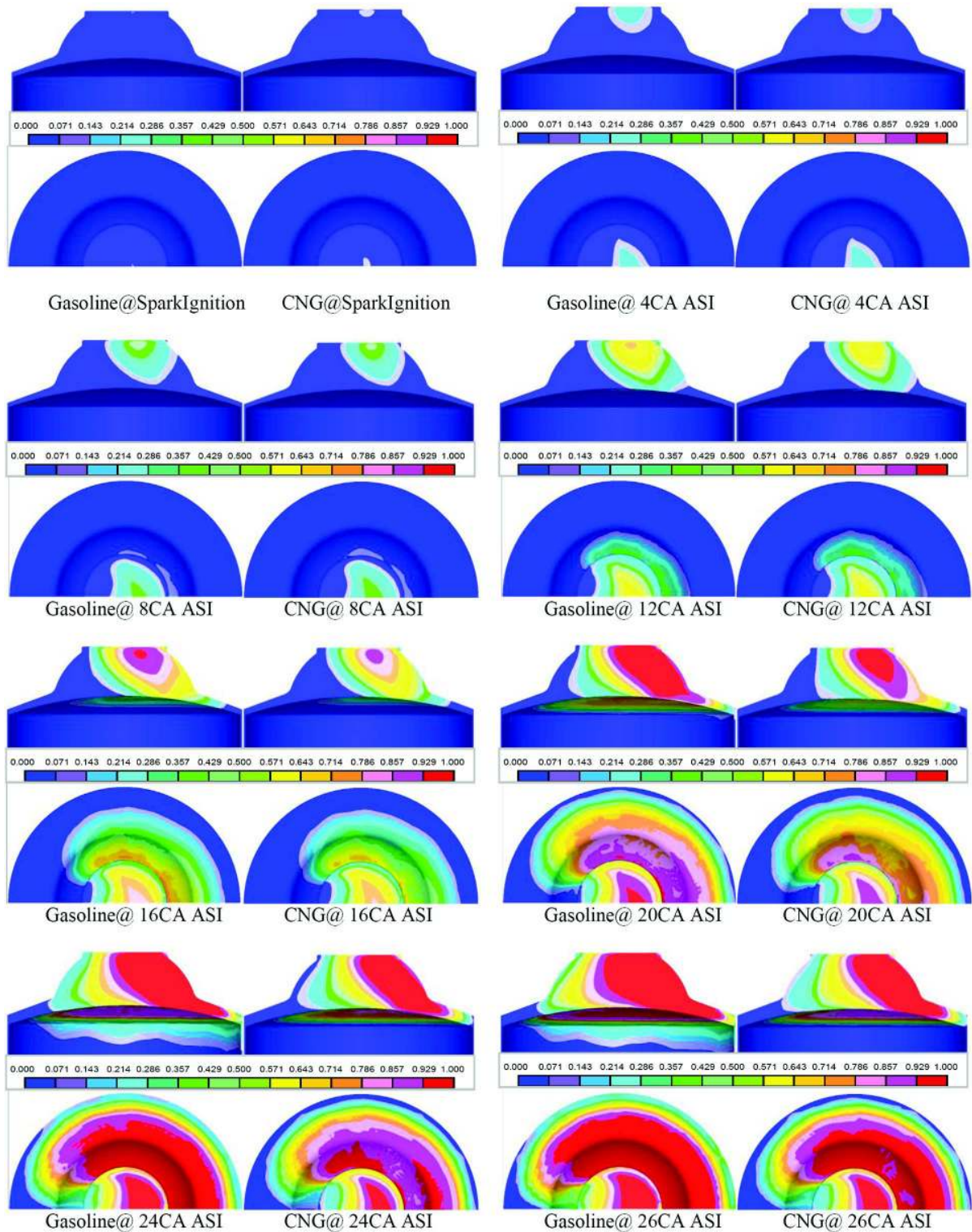
Figure 15. Combustion model progress variable field during combustion, Gasoline vs. CNG, 7000 rpm

both promoting a rapid increase of the flame kernel, as highlighted by the fast growth of the consumed fuel portion;

• the 5500 rpm case, despite being characterized by the lowest in-cylinder average temperature (783 K), shows a nearly-stoichiometric / slightly rich mixture composition

(λ=0.92) promoting the combustion early development. The two counteracting effects lead to the intermediate kernel growth speed visible in Figure 18;

• at 7000 rpm, the engine is operated under a very rich fuel mixture (λ=0.88), falling outside the optimum range, and in-cylinder temperature levels (830 K) are not sufficient to counterbalance the excessively rich composition at the spark plug, thus leading to the slowest flame development among the tested cases.
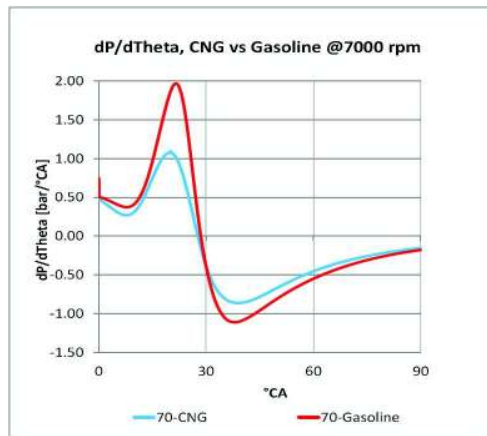

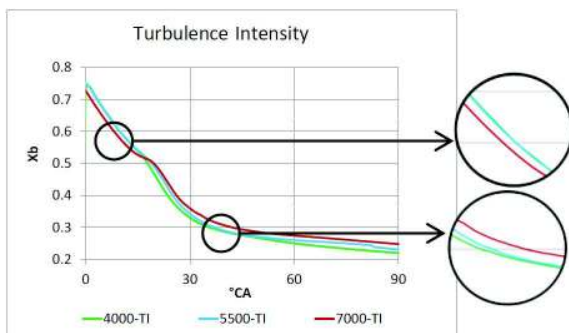**Figure 16. In-cylinder pressure derivative history, Gasoline vs. CNG, 7000rpm**

Figure 17. In-cylinder turbulence intensity, Gasoline, all engine revolution speed

Later during the combustion process, turbulent effects and local flow patterns start to play a primary role on the flame evolution and the burned/unburned gas mixing. As visible from Figure 18, starting from 24°CA ASI, the highest engine speed quickly closes the gap, while the lowest engine speed is not capable of involving the outer portion of the combustion chamber. As visible from the last set of pictures, towards the end of combustion a non-negligible portion of the chamber, whose amplitude decreases as the engine speed increases, is still filled with fresh fuel.

Knock analysis

From the experimental campaigns, an incipient knocking operation is detected with gasoline fuel, while no knocking occurrence is observed when fuelling the engine with CNG. To verify the experimental findings, a preliminary analysis is performed with the 1D knock model described earlier; then, a more refined investigation is carried out with 3D model, as well.

1D Results: spark advance and compression ratio variations

The knock index defined in eq. (9) is evaluated for 1D computed pressure cycles in the whole engine operating range for both fuels. Results reported in the Figure 19 below show that, apart from 4500 engine speed, exhibiting a more intense knocking, all the other Gasoline operated points present a knock index below the 2% threshold. As for the CNG-fuelled engine, the same numerical analysis clearly demonstrates a tremendous reduction in terms of knock probability, therefore allowing the engine to operate under more advanced spark timings and/or higher compression ratio.

A deeper investigation is carried out for Gasoline at 7000 rpm, standard spark equal to −11.5 °CA, where, basing on the previous results, a knock-free operation is expected. Figure 20 shows the knock-induced sharp rise of the unburned gas temperature occurring with just a 2° CA spark advance increase. This confirms that the experimental spark timing equal to 11.5 °CA BTDC can be considered as a knock-limit for gasoline operation at 7000 rpm. The zoomed area in the same figure also shows that, for a light knocking operation, say 1-4% of knock released heat, effects on in-cylinder pressure are almost undetectable by an experimental point of view.

Similar conclusion can be drawn looking at Figure 21, where the knock index is evaluated for several spark advance values, again for both fuels. In the case of Gasoline, the 2% threshold value is confirmed to be rapidly overcome for a spark advance greater than 11.5 °CA, while, for CNG, despite an expected small increase, the knock index is shown to remain greatly below the threshold value even for the highest spark advance and an increased compression ratio of 16.

Of course, the possibility to increase both compression ratio and spark advance allows to reduce the efficiency gap between CNG and Gasoline, as reported in Figure 22. As shown, gasoline operation is constrained far from the best efficiency point due to knocking (black thick line, Figure 22a). On the contrary, a knock-free operation and a radiated noise level below the previously defined limit is allowed in CNG operation up to the best efficiency points for the standard and increased compression ratios, as well (dashed thick lines in Figure 22b). In particular, at the standard compression ratio, the CNG fuelled engine can operate at an increased brake efficiency just changing the spark advance. Moreover, the efficiency can be further improved up to gasoline level of the original engine by increasing the compression ratio. In this way, although not completely recovered, the power output gap shown in Figure 10 is slightly reduced, too.
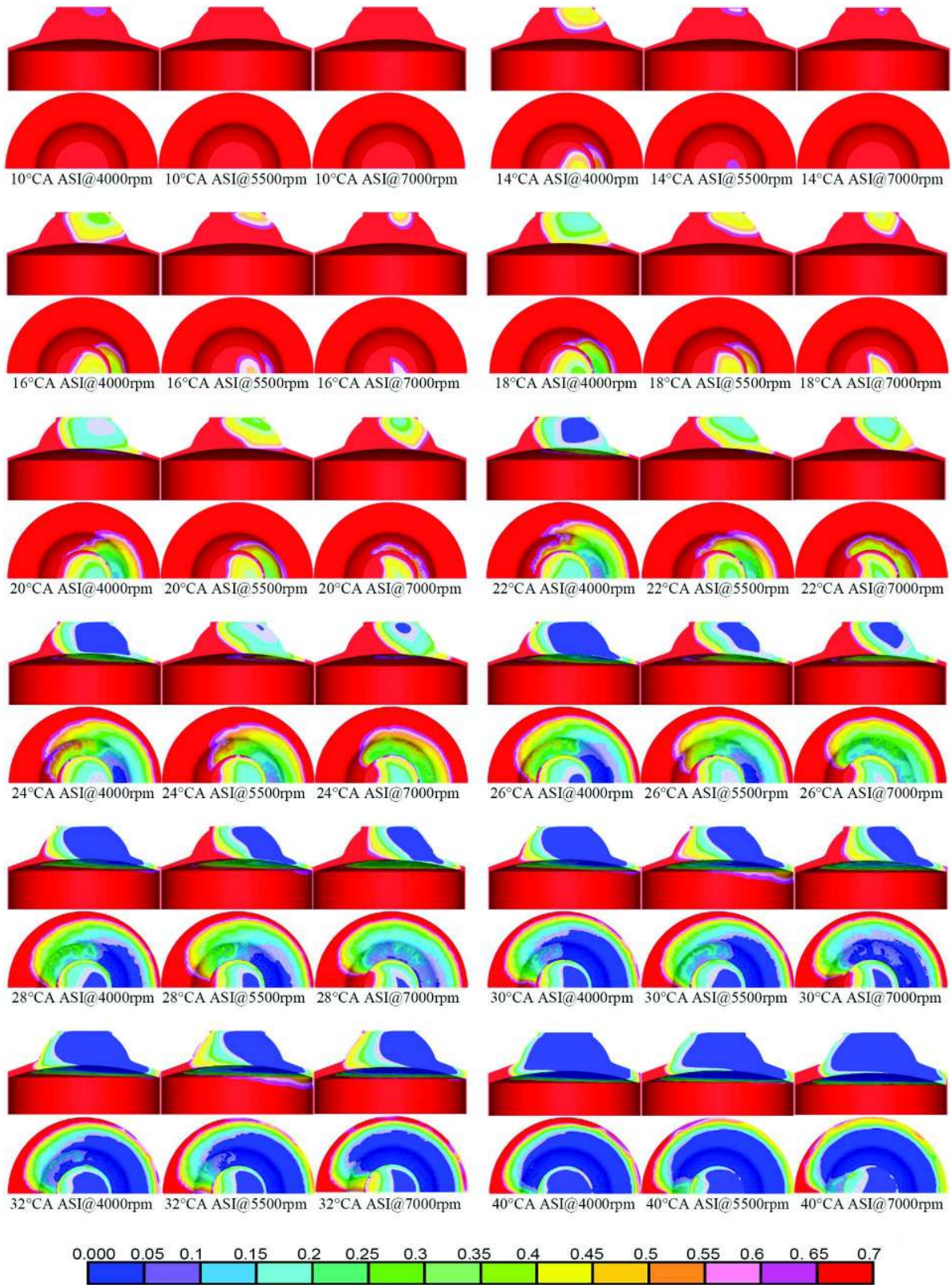
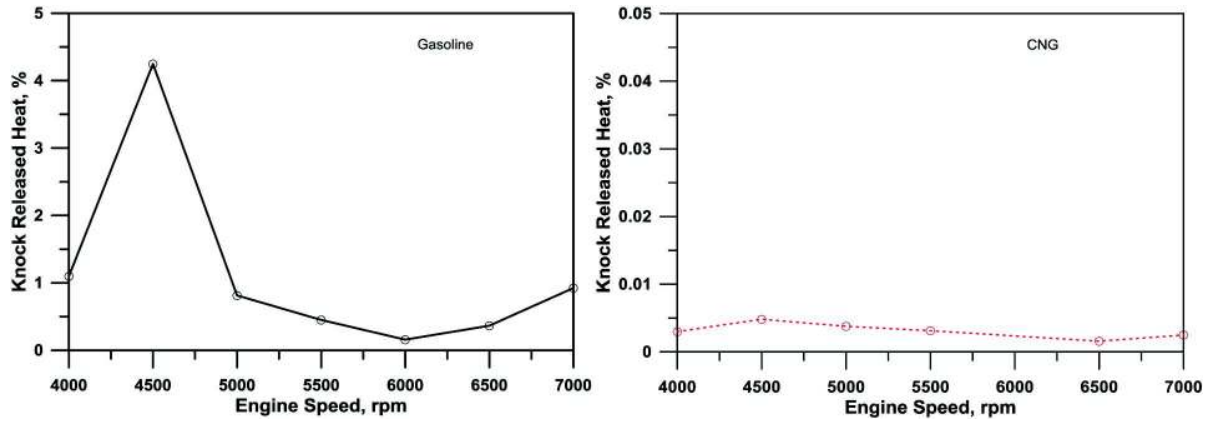*Figure 18. Comparison between gasoline field during combustion for all engine revolution speed*

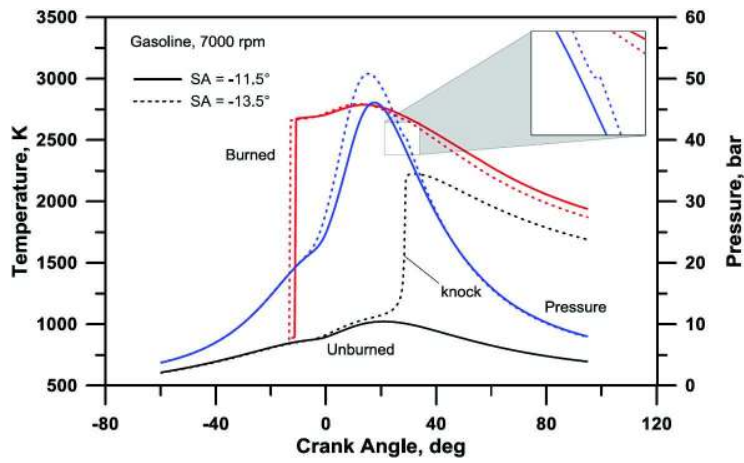**Figure 19. 1D knock index at various engine speeds for Gasoline and CNG**

Figure 20. Pressure and Temperature in the burned and unburned zones at incipient knocking conditions
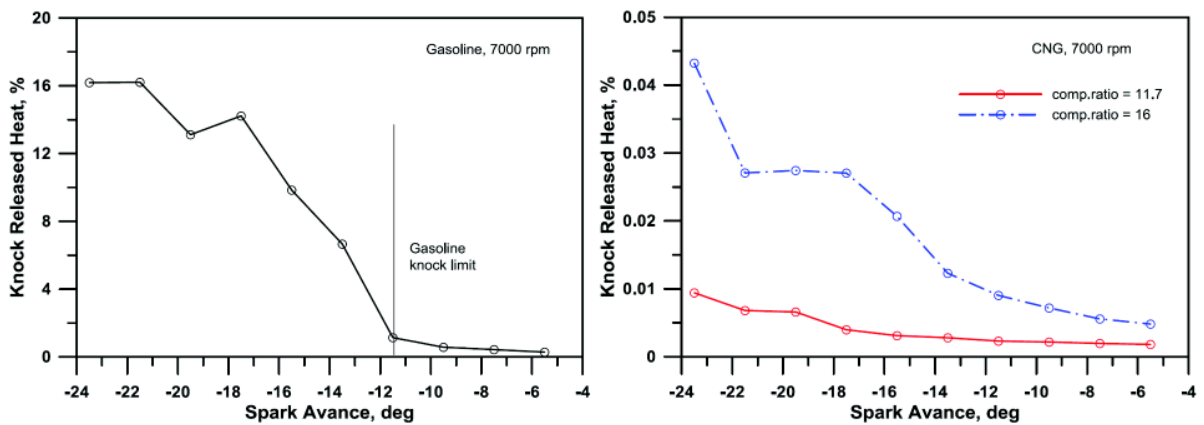

Figure 21. 1D knock index at various spark advances for Gasoline and CNG
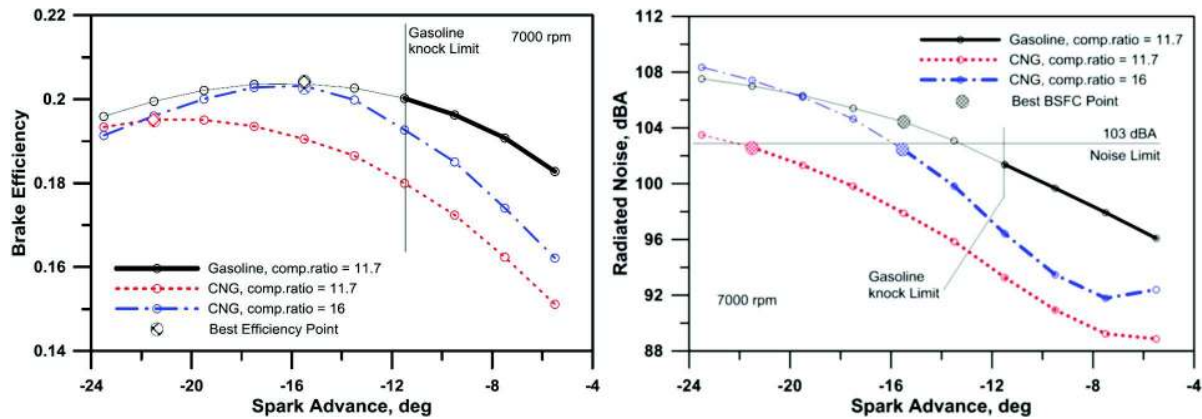
Figure 22. Brake Efficiency (a) and radiated noise (b) computed by the 1D model coupled to knock and acoustic procedures

3D results

Concerning the knocking operation, the above considerations are here confirmed by the 3D analyses of the combustion process and pointwise pressure evolution within the cylinder. Both CNG and gasoline operations of the engine are modeled, this time varying the spark advance in order to promote the onset of knocking and establish the knock-limited ignition timing. Among the many investigated cases, Figure 23 below shows results from three simulations for each fuel at 7000 rpm, where SA_0 is the reference Spark Advance equal to 11.5°CA BFTDC. The analysis of the picture clearly highlights the following issues:

• on one hand, considering the CNG operated engine, no knocking is detected even relevantly advancing the spark timing. This is a confirmation of the well-known high knock resistance of the natural gas, which could be proficiently used in order to counterbalance the reduced mass-specific energy of the fuel;

• on the other hand, knock-onset is clearly visible considering the gasoline operation of the engine, where it is possible to see that even small modifications to the reference spark advance lead to the occurrence of non-negligible knock during the second half of the combustion process;

• the same observations can be made if considering the pressure derivative reported in Figure 24, where the onset of steep pressure rises after TDC is observed for both the advanced spark timings for the sole gasoline operation.
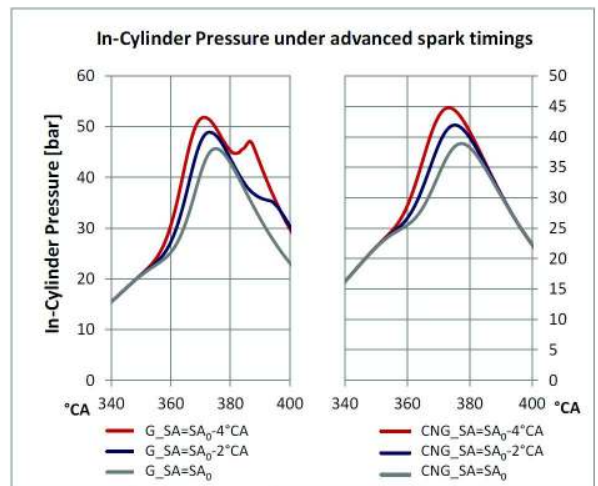

Figure 23. In-cylinder pressure under knock conditions, Gasoline vs. CNG, 7000 rpm.
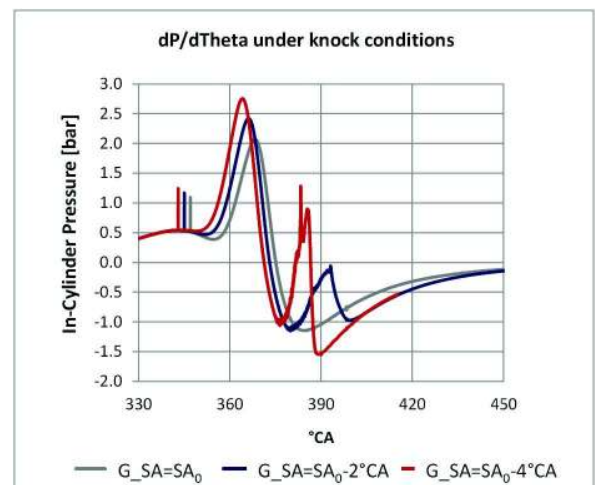

Figure 24. Pressure derivative history under knock conditions, Gasoline, 7000 rpm
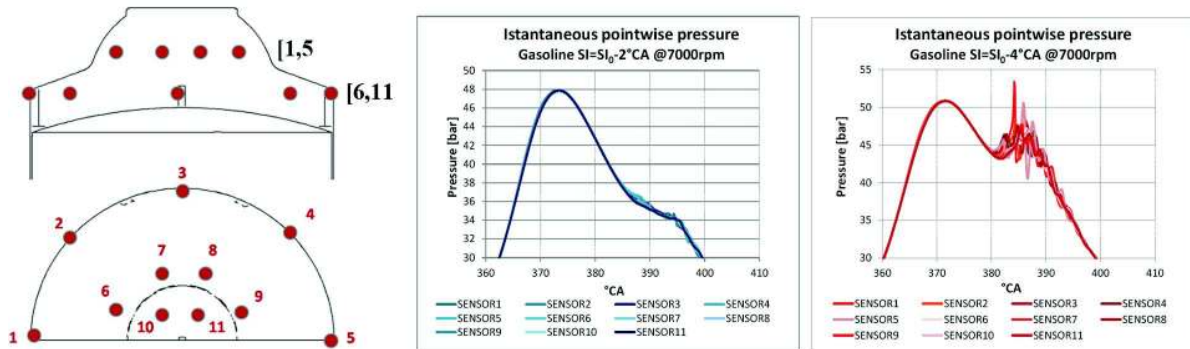
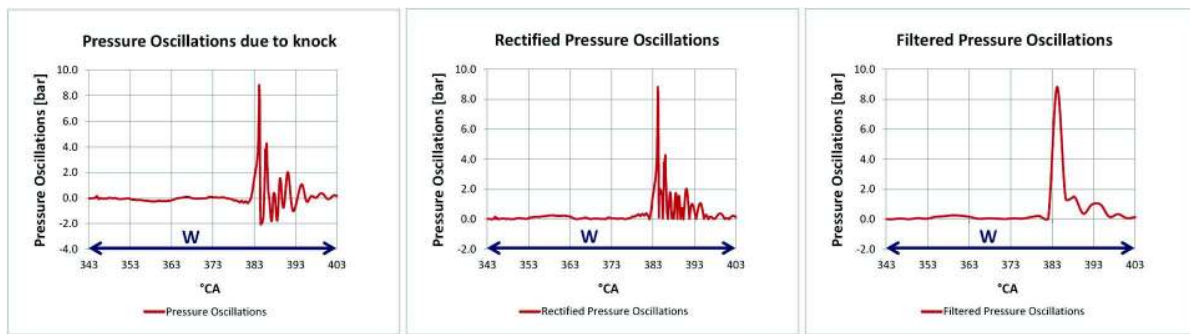*Figure 25. Knock-sensor locations and instantaneous pointwise pressure signals - Gasoline, 7000 rpm.*

Figure 26. Logical process for MAPO, IMPO and DKI calculation, 7000rpm, SI=SI0-4°CA, 20 kHz pass-band filter

In order to quantify the knock tendency for the modified spark timings, the previously described knock indices are computed adopting a pass-band frequency of 20 kHz, corresponding to nearly 2°CA for the maximum engine speed of 7000 rpm and a computational window of 60 °CA starting from the Spark Ignition. The analysis is now carried out moving from a global to a local perspective: Figure 25 shows the location of 11 pointwise virtual sensor used in the CFD analyses to post-process the local effects of incipient knock together in terms of local pressure signal, as well as the resulting computed pressure oscillations. The average in-cylinder pressure is omitted in order to better detect the local pressure signals.

As qualitatively described in Figure 26 below, the in-cylinder average pressure is at first subtracted to the most critical local value, in order to eliminate the pressure variation due to the standard combustion process. The resulting signal is then rectified and then filtered. Finally, *MAPO*, *IMPO* and *DKI* values are computed. The overall process for the specific $SI_0-4°CA$ case is reported in Figure 26 below.

Table 3 shows the resulting knock-tendency indices for the two advanced spark timings shown above: the intermediate SI_0-2°CA, having a *DKI* value of 0.239, closely approaches the critical lower limit of 0.2, while a further advancing of the spark timing leads to a non-acceptable *DKI* value of 0.06, thus confirming that the reference spark value

should be considered a limit value when taking into account cycle to cycle variability and the need for high engine life-cycle reliability.

Table 3. Calculated Knock tendency indices

	SA=SA$_0$-2°CA	SA=SA$_0$-4°CA
MAPO	0.589	8.821
IMPO	8.588	34.578
DKI	0.239	0.064

SUMMARY/CONCLUSIONS

A wide integrated numerical and experimental activity aiming at characterizing the behavior of a small displacement 2-stroke engine fuelled with gasoline and CNG is reported in the paper.

On the numerical side, both 1D and 3D tools are used to analyze the engine behavior in terms of both scavenging parameters and combustion over a wide range of operating conditions. The two numerical approaches are iteratively integrated until differences in terms of key-parameter predictions are negligible. Particular care is devoted to accurately model the combustion process: once a reliable characterization of the engine performance is achieved, the two simulation tools are used to assess the knock sensitivity of the engine to variations of some engine parameters (spark timing and compression ratio) and for both fuels. 1D results are also used to provide information on the engine

combustion radiated noise. Benefits from the integration of different modeling approaches are demonstrated and discussed, proving that the synergic use of different simulation tools allows the researchers to better understand and address the in-cylinder processes.

On the experimental side, a broad range of gasoline and CNG engine operations are investigated. Measurements in terms of engine performance, in-cylinder and port instantaneous pressure waves and scavenging characteristics are performed. Experiments are also used to tune and validate the above mentioned CFD models: once again, the integration of experimental and modeling techniques leads to a deeper comprehension of the engine performance and limitations.

Finally, a qualitative assessment of potential benefits and limitations of design and operating condition modifications in terms of engine performance and radiated noise is carried out for both gasoline- and CNG-fueled operations, and results are critically discussed through the synergic analysis of results from the above mentioned modeling approaches.

The results presented put into evidence the limitations induced by knocking phenomena for gasoline operation, while a knock-free operation is always ensured for CNG, even for high spark advance and compression ratio. This allows to improve fuel consumption of CNG operated engine and recover the initial efficiency gap, without increasing the radiated noise level of the original engine. As previously shown, in fact, the knock resistance of CNG allows the engine to reach the highest efficiency levels if natural gas is combined to an increase of both spark advance and compression ratio, without exceeding the radiated noise limit, thus resulting in an almost complete recovery of the well known power output gap of CNG versus gasoline.

REFERENCES

1. Manufacturers of Emission Controls Association, "Emission control of two- and three- Wheel Vehicles", 2008
2. Leighton, S., Cebis, M., Southern, M., Ahern, S. et al., "The OCP Small Engine Fuel Injection System for Future Two-Stroke Marine Engines," SAE Technical Paper 941687, 1994, doi: 10.4271/941687.
3. Duret, P., Ecomard, A., and Audinet, M., "A New Two-Stroke Engine with Compressed-Air Assisted Fuel Injection for High Efficiency low Emissions Applications," SAE Technical Paper 880176, 1988, doi: 10.4271/880176.
4. Nuti, M., Pardini, R., and Caponi, D., "FAST Injection System: PIAGGIO Solution for ULEV 2T SI Engines," SAE Technical Paper 970362, 1997, doi: 10.4271/970362.
5. Atkar, A., Tandan, V., Rairikar, S., Nair, C. et al., "Development Aspects of Conversion of 2-stroke Gasoline Engine to Operate on Bi-fuel CNG and Dedicated CNG Mode," SAE Technical Paper 962477, 1996, doi: 10.4271/962477.
6. Shanmugam, P., Anbukarasu, A., Babu, Y., Harne, V. et al., "Development of a 2-Stroke CNG Engine for 3-Wheeler Vehicle for the Indian Market," SAE Technical Paper 2009-26-0022, 2009, doi: 10.4271/2009-26-0022.
7. Mattarelli, E., Fontanesi, S., Gagliardi, V., and Malaguti, S., "Multidimensional Cycle Analysis on a Novel 2-Stroke HSDI Diesel Engine," SAE Technical Paper 2007-01-0161, 2007, doi: 10.4271/2007-01-0161.
8. Lavy, J., Angelberger, C., Guibert, P., and Mokhtari, S., "Towards a Better Understanding of Controlled Auto-Ignition (CAI™) Combustion Process From 2-Stroke Engine Results Analyses," SAE Technical Paper 2001-01-1859, 2001, doi: 10.4271/2001-01-1859.
9. Bozza, F., Gimelli, A., Fontanesi, S., and Severi, E., "1D and 3D CFD Investigation of Burning Process and Knock Occurrence in a Gasoline or CNG fuelled Two-Stroke SI Engine," SAE Technical Paper 2011-32-0526, 2011, doi: 10.4271/2011-32-0526.
10. GT-Power v.7.1 - Engine Performance Application Manual, Gamma Technologies, 2010
11. Blizard, N. and Keck, J., "Experimental and Theoretical Investigation of Turbulent Burning Model for Internal Combustion Engines," SAE Technical Paper 740191, 1974, doi: 10.4271/740191.
12. Matthews, R. and Chin, Y., "A Fractal-Based SI Engine Model: Comparisons of Predictions with Experimental Data," SAE Technical Paper 910079, 1991, doi: 10.4271/910079.
13. Yoshiyama, S., Tomita, E., Zhang, Z., and Hamamoto, Y., "Measurement and Simulation of Turbulent Flame Propagation in a Spark Ignition Engine by Using Fractal Burning Model," SAE Technical Paper 2001-01-3603, 2001, doi:10.4271/2001-01-3603.
14. Bozza, F. and Gimelli, A., "A Comprehensive 1D Model for the Simulation of a Small-Size Two-Stroke SI Engine," SAE Technical Paper 2004-01-0999, 2004, doi:10.4271/2004-01-0999.
15. North, G.L., and Santavicca, D.A., "The Fractal Nature of Premixed Turbulent Flames", Comb. Science and Tech., Vol. 72, pp. 215-232, 1990
16. Rhodes, D. and Keck, J., "Laminar Burning Speed Measurements of Indolene-Air-Diluent Mixtures at High Pressures and Temperatures," SAE Technical Paper 850047, 1985, doi: 10.4271/850047.
17. Bozza, F., Gimelli, A., and Tuccillo, R., "The Control of a VVA-Equipped SI Engine Operation by Means of 1D Simulation and Mathematical Optimization," SAE Technical Paper 2002-01-1107, 2002, doi:10.4271/2002-01-1107.
18. Bozza, F., Gimelli, A., Andreassi, L., Rocco, V. et al., "1D-3D Analysis of the Scavenging and Combustion Process in a Gasoline and Natural-Gas Fuelled Two-Stroke Engine," SAE Technical Paper 2008-01-1087, 2008, doi:10.4271/2008-01-1087.
19. Miller, D.S., Internal Flow Systems, Second Edition, BHR Group Limited, 1990
20. Bingham, J.F., and Blair, G.P. "An improved branched pipe model for multi-cylinder automotive engine calculations", Proc. of Inst. of Mech. Eng., Vol. 199, No D1, 1985
21. Warnatz, J., Maas, U., Dibble, R.W., "Combustion, Physical and Chemical Fundamentals, Modeling and Simulation, Experiments, Pollutant Formation", 4th Edition, Springer, 2006
22. Poulos, S. and Heywood, J., "The Effect of Chamber Geometry on Spark-Ignition Engine Combustion," SAE Technical Paper 830334, 1983, doi: 10.4271/830334.
23. Bozza, F., Fontana, G., Galloni, E., and Torella, E., "3D-1D Analyses of the Turbulent Flow Field, Burning Speed and Knock Occurrence in a Turbocharged SI Engine," SAE Technical Paper 2007-24-0029, 2007, doi:10.4271/2007-24-0029.
24. Blair, G.P., "Design and Simulation of Two-Stroke Engines," SAE International, Warrendale, PA, ISBN 978-1-56091-685-7, 1996, doi: 10.4271/R-161.
25. Heywood, J.B. and Sher, E., "The Two-Stroke Cycle Engine-Its Development, Operation, and Design," SAE International, Warrendale, PA, 1999.
26. Tanaka, S., Ayala, F., Keck, J., "A Reduced Chemical Kinetic Model for HCCI Combustion of Primary Reference Fuels", Combustion & Flame, 132, pp. 219-239, 2003.
27. Smith, Gregory P., Golden, David M., Frenklach, Michael, Moriarty, Nigel W., Eiteneer, Boris, Goldenberg, Mikhail, Bowman, C. Thomas, Hanson, Ronald K., Song, Soonho, Gardiner, William C.Jr., Lissianski, Vitali V., and Zhiwei, Q, in http://www.me.berkeley.edu/gri_mech/
28. Scarpati, J., Wikström, A., Jönsson, O., Glav, R. et al., "Prediction of Engine Noise using Parameterized Combustion Pressure Curves," SAE Technical Paper 2007-01-2373, 2007, doi:10.4271/2007-01-2373.
29. Siano, D., Bozza, F., and Costa, M., "Reducing Fuel Consumption, Noxious Emissions and Radiated Noise by Selection of the Optimal Control Strategy of a Diesel Engine," SAE Technical Paper 2011-24-0019, 2011, doi:10.4271/2011-24-0019.
30. Angelberger, C., Poinsot, T., and Delhay, B., "Improving Near-Wall Combustion and Wall Heat Transfer Modeling in SI Engine Computations," SAE Technical Paper 972881, 1997, doi: 10.4271/972881.
31. Duclos, J.M., Zolver, M., and Baritaud, T. 1999. '3D modeling of combustion for DI-SI engines', Oil & Gas Science and Technology - Rev.IFP, 54(2), pp. 259-264.
32. Colin, O. and Benkenida, A. "The 3-Zones Extended Coherent Flame Model (ECFM3Z) for Computing Premixed/Diffusion Combustion" Oil & Gas Science and Technology - Rev. IFP, Vol. 59 (2004), No. 6, pp. 593-609
33. Colin, O., Pires da Cruz, A. and Jay, S. 2004. 'Detailed chemistry bases auto-ignition model including low temperature phenomena applied to 3D engine calculations', 30th Symposium (International) on Combustion, The Combustion Institute
34. Brecq, G., Bellettre, J., Tazerout, M. "A new indicator for knock detection in gas SI engines" Int.l Journal of Thermal Sciences
35. Diana, S., Giglio, V., Iorio, B., and Police, G., "Evaluation of the Effect of EGR on Engine Knock," SAE Technical Paper 982479, 1998, doi: 10.4271/982479.

ACRONYMS AND ABBREVIATIONS

1D
One Dimensional
3D
Three Dimensional
ABDC
After Bottom Dead Center
AFTDC
After Firing Top Dead Center
AMG
Algebraic Multi Grid
ASI
After Spark Ignition
BDC, TDC
Bottom, Top Dead Center
BBDC
Before Bottom Dead Center
BFTDC
Before Firing Top Dead Center
BSFC
Brake Specific Fuel Consumption
CA
Crank Angle
CE
Charging Efficiency
CFD
Computational Fluid Dynamics
CNG
Compressed Natural Gas
DR
Delivery Ratio
DAQ
Data Acquisition
DC
Direct Current
DKI
Dimensionless Knock Indicator
ECFM-3Z
3-Zones Extended Coherent Flame Model
Exp
Experimental
GR
Exhaust Gas Recirculation
FTDC
Firing Top Dead Center
GDI
Gasoline Direct Injection
IMEP
Indicated Mean Effective Pressure
IMPO
Integral of Modulus of Pressure Oscillations
IC
Internal Combustion
LHV
Lower Heating Value
MAPO
Maximum Amplitude of Pressure Oscillations
MARS
Monotone Advection and Reconstruction Scheme
N
Engine Speed
NG
Natural Gas
RC
Compression Ratio

RE
Retaining Efficiency
RON
Research Octane Number
R&D
Research and Development
SA
Spark Advance, Structure Attenuation
SA$_0$
Reference Spark Advance
SE
Scavenging Efficiency
SPL
Sound Pressure Level
WOT
Wide Open Throttle
W
Computational Window

NOMENCLATURE

Latin
a, b, c, g
Constants in ECFM-3Z Knock Model
A_L
Laminar Flame Surface
A_T
Turbulent Flame Surface
C_p
pressure loss coefficient
c_{pu}
Unburned Gas Specific Heat at Constant Pressure
D
Duct diameter / Destruction Term
D_3
fractal dimension
e_i
Internal Energy of the i-th specie
E
Total Energy per unit mass
F
Flux Term
f
friction coefficient
H
Total Enthalpy per unit mass
k
Kinetic Energy of Turbulent Flow Field
K
Kinetic Energy of the mean Flow Field
L
duct length
LHV
Lower Heating Value
L_{max}
maximum turbulent length scale
L_{min}
minimum turbulent length scale
m_b
gas burned mass
m_f
Fuel Mass
m_u
gas unburned mass

$M_{cyl, tr}$
Total Mass trapped in the Cylinder

$M_{f, tr}$
Fresh Charge trapped in the Cylinder

$\dot{m}$
Mass Flow Rate

$\dot{m}_{ex}$
Exhaust Mass Flow Rate

$\dot{m}_{in}$
Intake Mass Flow Rate

N_{spec}
Total Number of the i-th species

p, P
Pressure

q
rate of heat exchange

Q_{chem}
Chemical Reaction Heat

Q_{ub}
Total Heat released in the Unburned Gases

Q_w
Wall Exchange Heat

S
Source Term

S_L
Laminar Flame Speed

t
Time

T_u
Unburned Gas Zone Temperature

u
Flow Velocity

U
Conservative Variables Vector

U_f
mean Flow Field velocity

u'
turbulence intensity velocity

V_c
Engine Displacement

V_u
Unburned Gas Volume

x
duct arc length

$x_{f, YTF}$
fuel fraction

x_i
Composition of the i-th specie

x_r, Y_{egr}
residual gas fraction

x_{Qub}
Normalized Heat released in the Unburned Gases

YIG
3D Knock Parameter

Latin subscripts

f, in
Fresh Charge to the Cylinder through the Transfer Ports

f, ex
Fresh Charge exiting out of the Cylinder

Greeks

η_{ch}
Charging Efficiency

η_{sc}
Scavenging Efficiency

η_v
Retaining Efficiency

λ
Air Index

Λ
Delivery Ratio

ρ
Gas Density

ρ_u
Unburned Gas Density

ρ_{amb}
Ambient Air Density

Ω
duct area

CONTACT INFORMATION

Stefano Fontanesi (Assistant Professor)
Elena Severi (PhD student)
Department of Mechanical and Civil Engineering (DIMeC)
University of Modena
Via Vignolese 905 - 41122 Modena (Italy)
Ph. +39 059 2056114 -
Fax: +39 059 2056126
stefano.fontanesi@unimore.it
elena.severi@unimore.it

Fabio Bozza (Full Professor)
Alfredo Gimelli (Assistant Professor)
Department of Mechanical Engineering (DIME)
University of Naples "Federico II"
Via Claudio 21, 80125 Napoli (Italy)
Ph. +39 081 7683274 / 71 -
Fax: +39 081 2394165
fabio.bozza@unina.it
alfredo.gimelli@unina.it

Daniela Siano (researcher)
Noise and Vibration Department
Istituto Motori, CNR
Via Marconi, 8 - 80125, Napoli
d.siano@im.cnr.it

APPENDIX

APPENDIX A

Delivery ratio (*DR*)

$$\Lambda \overset{def}{=} \frac{\int \dot{m}_{f,in} \, dt}{\rho_{amb} * V_c}$$

<div align="right">(A1)</div>

Charging efficiency (*CE*)

$$\eta_{ch} \overset{def}{=} \frac{\int \dot{m}_{f,in} dt - \int \dot{m}_{f,ex} dt}{\rho_{amb} * V_c}$$

<div align="right">(A2)</div>

Retaining efficiency (*RE*) (or Trapping Efficiency)

$$\eta_v \overset{def}{=} \frac{\int \dot{m}_{f,in} dt - \int \dot{m}_{f,ex} dt}{\int \dot{m}_{f,in} dt} = \frac{\eta_{ch}}{\Lambda}$$

<div align="right">(A3)</div>

Scavenging efficiency (*SE*)

$$\eta_{sc} = \frac{M_{f,tr}}{M_{cyl,tr}}$$

<div align="right">(A4)</div>